# Cross-sectional characterization of the conversion layer formed on AA2024-T3 by a lithium-leaching coating

Kosari, A.; Visser, P.; Tichelaar, F.; Eswara, S.; Audinot, J. N.; Wirtz, T.; Zandbergen, H.; Terryn, H.; Mol, J. M.C.

**DOI**
10.1016/j.apsusc.2020.145665

**Publication date**
2020

**Document Version**
Final published version

**Published in**
Applied Surface Science

**Citation (APA)**
Kosari, A., Visser, P., Tichelaar, F., Eswara, S., Audinot, J. N., Wirtz, T., Zandbergen, H., Terryn, H., & Mol, J. M. C. (2020). Cross-sectional characterization of the conversion layer formed on AA2024-T3 by a lithium-leaching coating. *Applied Surface Science*, *512*, Article 145665. https://doi.org/10.1016/j.apsusc.2020.145665

Applied Surface Science 512 (2020) 145665

Contents lists available at ScienceDirect

Applied Surface Science

journal homepage: www.elsevier.com/locate/apsusc

Full Length Article

# Cross-sectional characterization of the conversion layer formed on AA2024-T3 by a lithium-leaching coating

A. Kosari[a], P. Visser[b], F. Tichelaar[c], S. Eswara[d], J-N. Audinot[d], T. Wirtz[d], H. Zandbergen[c], H. Terryn[a,e], J.M.C. Mol[a,*]

[a] Delft University of Technology, Department of Materials Science and Engineering, Mekelweg 2, 2628 CD Delft, the Netherlands
[b] AkzoNobel, Expertise Center Corrosion, Rijksstraatweg 31, 2171 AJ Sassenheim, the Netherlands
[c] Delft University of Technology Quantum Nanoscience, Kavli Institute of Nanoscience, Lorentzweg 1, 2628 CJ Delft, the Netherlands
[d] Luxembourg Institute of Science and Technology (LIST), Advanced Instrumentation for Ion Nano-Analytics (AINA), Materials Research and Technology Department, 41, rue du Brill, L-4422 Belvaux, Luxembourg
[e] Vrije Universiteit Brussel, Department of Materials and Chemistry, Research Group Electrochemical and Surface Engineering (SURF), Pleinlaan 2, 1050 Brussels, Belgium

ARTICLE INFO

*Keywords:*
Leachable lithium carbonate
Layered double hydroxide
AA2024-T3
High Resolution TEM
Energy Filtered TEM
SIMS

ABSTRACT

This work focuses on the cross-sectional characterization of the protective conversion layer formed on AA2024-T3 by lithium-leaching from a polyurethane coating in a corrosive environment. The layer shows a multi-layered arrangement comprising nanoscopic local phases. Transmission electron microscopy (TEM) and complementary high-resolution secondary ion mass spectroscopy (SIMS) were employed to observe the cross-sections of the entire layer formed at different locations of a 1-mm-wide scribe, in terms of morphology, structure and chemical composition. The conversion layer was comprised of two ubiquitous sublayers; a thin dense layer (i.e. 150 nm) adjacent the alloy substrate and a porous layer. The former represents an amorphous lithium-containing pseudoboehmite phase, Li-pseudoboehmite, whereas the latter is composed of amorphous and crystalline products; an outer columnar layer merely seen on the peripheral region is also crystalline. Through a sandwich structure and the $d_{(003)}$ basal spacing, the crystalline phases were identified as Li-Al layered double hydroxide. Although lithium was found uniformly spread within different regions, the local phases with no/low concentration of lithium were revealed with energy filtered TEM and confirmed with SIMS analysis.

## 1. Introduction

A high strength-to-weight ratio is a key characteristic that has made aluminum alloy (AA) 2024-T3 attractive for aerospace applications. However, its high susceptibility to localized corrosion because of a heterogeneous microstructure is a downside of this alloy [1–3]. For many decades, hexavalent chromium-containing compounds have been applied reliably for conversion surface treatments and active protective coating pigmentation [4–6]. However, international health and safety legislation is imposing restrictions on their utilization, demanding the development of new corrosion inhibitive systems with reduced ecological footprints. This requires researchers either to establish new corrosion mitigation strategies or introduce new inhibitor compounds, providing equal or better active protection as compared to the existing chromated systems [7,8].

In the early 1990s, lithium salts dissolved in alkaline solutions were reported to stabilize aluminum hydroxide through lithium intercalation, showing a corrosion inhibitive character for aluminum and its alloys [9–11]. In 1996, Drewien et al. proposed an alkaline lithium carbonate-lithium hydroxide bath, which favored the hydrotalcite formation over aluminum hydroxides, as a promising alternative to chromate conversion coatings [12]. Later, Visser and Hayes patented the use of lithium-salts as a leachable corrosion inhibitor when incorporated in organic coatings to provide active corrosion protection [13]. Visser and his co-workers demonstrated that a protective layer was generated from these lithium-leaching coatings. Thereafter, the studies were focused on the characterization, formation mechanism and corrosion protection properties of the conversion layer formed in artificially-damaged areas from lithium-leaching model coatings using chemical and electrochemical characterization techniques [14–16].

In an earlier work, Visser et al. reported that leaching of lithium-salts from the coating matrix can establish an alkaline environment (pH 9–10) within the defect area, facilitating the formation of a conversion layer on AA2024-T3 [17]. In fact, gradual leaching can induce a

* Corresponding author.
*E-mail address:* J.M.C.Mol@tudelft.nl (J.M.C. Mol).

https://doi.org/10.1016/j.apsusc.2020.145665
Received 9 October 2019; Received in revised form 10 January 2020; Accepted 4 February 2020
Available online 05 February 2020

ranging local electrolyte chemistry in the scribe, resulting in the formation of different conversion layer morphologies with exposure time. Furthermore, the crystallographic orientation of grains at the surface of the underlying metal alloy microstructure plays a role as well [17]. In terms of composition, the results suggested formation of an Li-Al layered double hydroxide (LDH) structure over an aluminum hydroxide gel [17]. The layer, albeit morphologically diverse, is capable to protect the aluminum substrate in aggressive environments like neutral salt spray (NSS) conditions [16]. The morphology of the conversion layer shows a multi-layered structure composed of two ubiquitous layers; a dense layer adjacent the alloy substrate and a porous layer. A columnar outer layer is also observed in the peripheral region of the scribe as a consequence of higher local pH and lithium concentration [14]. Electrochemical impedance spectroscopy studies revealed that the inner dense layer is the main contributor to the overall corrosion protection provided by the conversion layer while the porous and columnar layers contribute only to a minor extent [18].

Although previous studies have shown that lithium plays a determinative role in the layer formation, the full characterization of the layer has been challenging as lithium is hard to detect within such conversion layers. Lithium has very low characteristic X-ray energy and this causes limitations to detect it even with windowless energy dispersive spectroscopy (EDS) detectors on TEM. Auger electron spectroscopy (AES) can detect lithium, however it cannot be used for the current system as the lithium peak overlaps with the binding energy of aluminum oxide. X-ray photoelectron spectroscopy (XPS) analysis is restricted by a low sensitivity (about 1%wt detection limit) toward lithium and additionally a low lateral resolution to differentiate the dissimilar phases of a surface area. Visser et al. have used XPS, detecting 4.5–4.8 at.% lithium just at the surface of the conversion layer, that was associated with Li-Al LDH [17]. However, lithium might be present also in the inner parts of the layer either below the XPS detection threshold or removed while sputtering the top part, hence remaining undetected. Recently, Marcoen et al. employed time-of-flight secondary ion mass spectrometry (ToF-SIMS) to follow the generation of the protective conversion layer within a 1-mm-wide scribe as a function of Li-leaching time in a corrosive environment [19]. They reported that initially a hydrated aluminum oxide surface layer with a little incorporated lithium is formed upon exposure, which laterally grows as a result of further Li-leaching. Subsequently, a columnar deposit, with likely an LDH structure, can nucleate when the lithium concentration surpasses a certain threshold in the coating defect. Nevertheless, all the time-resolved information is collected from the near-top surfaces which provide no cross-sectional chemical insights into the mature layer. In spite of the mobile character of lithium to the electron beam [20,21], energy filtered transmission electron microscopy (EF-TEM) technique can be used to map lithium at a high resolution. Following that analysis approach, Liu et al. [14] detected lithium in different parts of the conversion layer with EF-TEM. However, owing to the difficulties preparing the TEM specimens out of different locations in the deep scribe, the cross-sections of the entire layer were not studied to observe the lithium distribution. In addition, high resolution TEM (HR-TEM) examinations to structurally characterize the local phases were not conclusive, likely caused by the destructive influence of the used electron beam on the structure. That is why the lithium conversion layer which spatially comprises many sub-micron local phases has not completely been described in terms of composition and structure, yet. This information is of great importance to fully elucidate the formation mechanism of the conversion layer within the scribe.

This work is aimed to fully characterize the protective layer on a morphological, structural and chemical level. Therefore, TEM is utilized to study the protective conversion layer generated from lithium-leaching coatings as this technique allows to produce chemical and structural images at nanometric and atomic level. The analytical TEM investigations including HR-TEM imaging, selected area electron diffraction (SAED) patterns, EF-TEM and EDS analysis are carried out on the cross-sections of the entire layer obtained by a dedicated focused ion beam (FIB) sample preparation procedure. Complementarily, cross-sectional elemental maps of the layer are acquired through high-resolution SIMS. The findings obtained in this study reveals spatial distribution of lithium within different nanoscopic parts where the local phases are structurally characterized as well.

**Table 1**
Composition of the model organic coatings.

| | Type | Supplier | Amount (g) |
|---|---|---|---|
| Component A | N-Butylacetate | Sigma–Aldrich | 75.0 |
| | Desmophen 650 MPA | Bayer materials science | 47.7 |
| | Lithium carbonate | Sigma–Aldrich | 23.6 |
| | Magnesium oxide | Sigma–Aldrich | 16.4 |
| | TiOxide TR 92 | Huntsman | 5.9 |
| Component B | Tolonate HDB 75 MX | Vencorex | 28.5 |
| | Dynasilan Glymo | Evonik | 5.2 |

## 2. Materials and methods

The coating was formulated as a white opaque primer using the compounds listed in Table 1 [22]. Polyurethane was used as the polymer matrix as its chemistry shows no interaction with discrete particulate ingredients in the primer preventing interference with the leachability of the lithium carbonate corrosion inhibitor [23]. The lithium-salt loaded coatings have a total pigment volume concentration (PVC) of 30 vol%, comprising 15 vol% inorganic pigments and fillers and 15 vol% lithium carbonate, respectively. The same procedure as reported already elsewhere was used for the coating preparation [14]. AA2024-T3 sheets, provided by Arconic, with a thickness of 0.8 mm were used as the substrate. The substrate was pre-treated by a tartaric sulfuric acid (TSA) anodizing process using a potential of 15 V for 25 min at 43 °C, leading to an anodic film of 3–3.5 μm, according to aerospace application requirements (AIPI 02–01-003). Coatings were applied with a high volume low pressure (HVLP) spray gun followed by a 1-h flash-off at 23 °C and curing at 80 °C for 16 h. The dry coating thickness was 20 to 25 μm. The coated panels, with dimensions of 7 cm × 7 cm, were damaged intentionally (St. Andrews cross) with a carbide steel milling blade, creating 1-mm-wide scribes penetrating 100–150 μm into the metal. Prior to placing the panels in the salt spray chamber, their backs and sides were masked with a polyester tape. The panels were exposed to a 5% (w/w) NaCl neutral salt spray (NSS) environment (ASTM-B117) for 168 h. After the exposure, the samples were rinsed with flowing deionized water for 2 min in order to quench the process and remove any chloride residues.

For TEM investigations, the thin cross-sections of the entire layer were fabricated successfully from the regions of interest by means of a Thermo Fisher Helios G4 FIB and lift-out procedure. Prior to gallium ion milling, top-view appearances of the conversion layer were first examined using 2-keV secondary-electron scanning electron microscopy (SE-SEM) observations. To protect the conversion layer from gallium damage, a layer of carbon was initially deposited with the electron beam, followed by Pt deposition with the Ga ion beam (see Supplementary Fig. 1). A Tecnai F20ST/STEM 200 kV was used for typical bright-field TEM imaging and scanning transmission electron microscopy/energy dispersive spectroscopy (STEM/EDS) elemental mapping. A Titan cubed Cs-corrected 300 kV, equipped with a direct electron (DE-16) camera, was employed for conducting high resolution TEM (HR-TEM) imaging at a low dose rate, i.e. 19 e/Å$^2$s. To map lithium within the conversion layer, the Li K-edge was energy-filtered by inserting 6-eV slits before and after the corresponding edge (EF-TEM jump-ratio approach) at either 80 or 300 keV. The identical procedure was used to filter the Al $L_{2,3}$-edge with an onset at $\Delta E = 73$ eV. To do so, the same electron dose rate as HR-TEM was used but the exposure

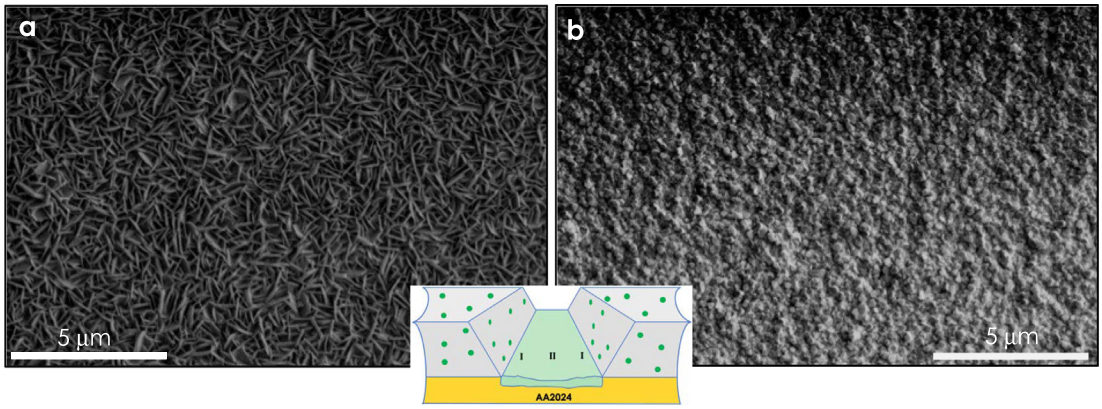


**Fig. 1.** Top-view SEM images of the conversion layer formed at the different regions of the scribe; (a) the peripheral part as Region I and (b) the middle part as Region II are denoted schematically in the inset.

time increased up to 60 s for acquiring sufficient counts.

High-resolution secondary ion mass spectroscopy (SIMS) imaging was performed in a helium ion microscope (HIM) (Zeiss, Peabody, MA, USA) coupled with a mass spectrometer [24–26]. To avoid edge effects during the SIMS analysis, the cross-section samples were embedded in Wood alloy. The SIMS images were acquired using 20 keV $Ne^+$ primary ion with a probe current of 3 pA, leading to a probe size in the range 20–40 nm. The raster size was from 5 × 5 $\mu m^2$ to 10 × 10 $\mu m^2$ with a matrix of 512 × 512 $pixels^2$. The sample stage was biased to +500 V to allow the detection of positive secondary ions. The parallel detection capability of the SIMS spectrometer enables the detection of several masses simultaneously; the secondary ions detected were $^7Li^+$, $^{24}Mg^+$ and $^{27}Al^+$.

## 3. Results and discussion

In general, the layer can be recognized by two predominant top-view morphologies; as shown in Fig. 1. The layer formed in the peripheral area (Region I) appears with a petal-like top view whereas the middle region (Region II) appearance shows globular features. A mixed morphology is observed normally while passing from the peripheral to the middle region (see Supplementary Fig. 2). In fact, the conversion layers are cross-sectionally different in morphology, including various local phases that are yet to be fully identified.

### *3.1. Cross-sectional characterization of the layer formed in the peripheral region*

A typical cross-sectional morphology of the layer formed at the peripheral region of the scribed area is revealed by TEM micrography, as shown in Fig. 2a. The thickness of the layer is approx. 1 µm. It should be noted that the outer region of the scribe is the area where a higher alkalinity and lithium concentration is probable due to the leaching process from the coating [19]. The cross-section reveals a multi-layered morphology which is comprised of three distinct sublayers; a 150-nm-thick dense layer with roundish porosities on the substrate, a 700-nm-thick columnar layer on the top and a thin porous layer in between.

HR-TEM observations of the columnar part of the layer reveal a local sandwich structure [27], directly referring to a layered double hydroxide (LDH) structure which can be characterized through the $d_{(003)}$ basal spacing of its hexagonal structure (see Fig. 2b) [28–30]. The $d_{(003)}$ basal spacing corresponds to the stacking sequence symmetry; however, this spacing is highly dependent on the type of intercalated anions [31]. In Fig. 2b, in areas with lattice spacing, numerous crystal imperfections are observed (circled in Fig. 2b), leading to varied values of the d spacing (i.e. 7.4–8.2 Å). In order to extract further structural information, attempts were made to record magnified images in a low dose condition, but the layer was rapidly evolving due to removal of interlayer water with the electron beam (see Supplementary Fig. 3). The observed lattice spacing corresponds well to the $d_{(003)}$ spacing in hydrotalcite (i.e. 7.62 Å) reported by Drewien et al. [12] and Hou et al. [36]. However, the chloride intercalation is also feasible as it can reportedly give rise to a slight increase in the d spacing (i.e. 7.8 Å) [36]. For the current system, the formation of $LiAl_2$-$CO_3$ LDH (i.e. $[LiAl_2(OH)_6](CO_3)_{0.5}{\cdot}nH_2O$) is most plausible. It has been reported that $CO_3^{2-}$ and $H_2O$ co-exist in the interlayer spacing (anionic part) whereas $Al^{3+}$, $Li^+$ and $OH^-$ are present in the (0 0 3) plane [29,32–37]. However, chloride might also be accommodated in the anionic interlayer spacing and thus $[LiAl_2(OH)_6]Cl{\cdot}nH_2O$ or $[Li_{0.99}Al_{2.01}(OH)_6](CO_3)_{0.44}Cl_{0.01}{\cdot}nH_2O$ can be established [36]; as depicted in the inset in Fig. 2b. Please note that the coated panels were exposed to NSS environment and a minor amount of chloride (~1.3 At %) is detected within the layer with EDS analysis (see Supplementary Fig. 6). In addition, lithium in the LDH sheets might partially be replaced with magnesium that exists in the conversion layer (~1.2 At%); this might cause a rise in the d spacing as well [36]. To avoid any confusion, they are all defined as Li-Al LDH in this work.

A closer look at the porous layer shows that the porous structure is comprised of amorphous and crystalline products (Fig. 2c). Measuring the d spacing indicates the presence of Li-Al LDH at some parts of the porous layer, but in a dissimilar morphology than the columnar layer. In addition, the $d_{(003)}$ spacing can also be recognized in the local Fast Fourier Transform (FFT) of different parts in the image. The dense layer represents an amorphous structure, revealing no interference spots in the FFT of the image (see Fig. 2d). However, care should be taken not to turn the amorphous layer into a nano-crystalline one by exposure to a high-dose electron beam, as shown in Supplementary Fig. 4.

To map lithium, electron energy loss spectroscopy (EELS) spectra were initially collected from the layers formed in the peripheral and middle region; Li K-edge clearly shows up as illustrated in Supplementary Fig. 5. Energy filtered TEM (EF-TEM) was used to map lithium and aluminum; other elements including Mg, Cl, C and O are also detected within the layer with EDS analysis and presented in Supplementary Fig. 6. Due to the presence of an extended Plasmon peak, jump-ratio EF-TEM imaging in which the intended element is mapped through dividing the Li K-edge filtered image by the pre-edge filtered image was performed instead of normal elemental mapping with two pre-edge slits [26]. In addition, STEM/EELS mapping was also not feasible, because of perforation of the layer by the electron beam while collecting the spectrum at the required dwell time. The EF-TEM results are shown in Fig. 3. Comparing the Li and Al maps in Fig. 3a, lithium is uniformly distributed throughout the conversion layer, in particular within the dense layer. However, the local aluminum hydroxides with no/low concentration of lithium are also revealed in the top part of the layer, indicated by the yellow arrows in Fig. 3a. A closer

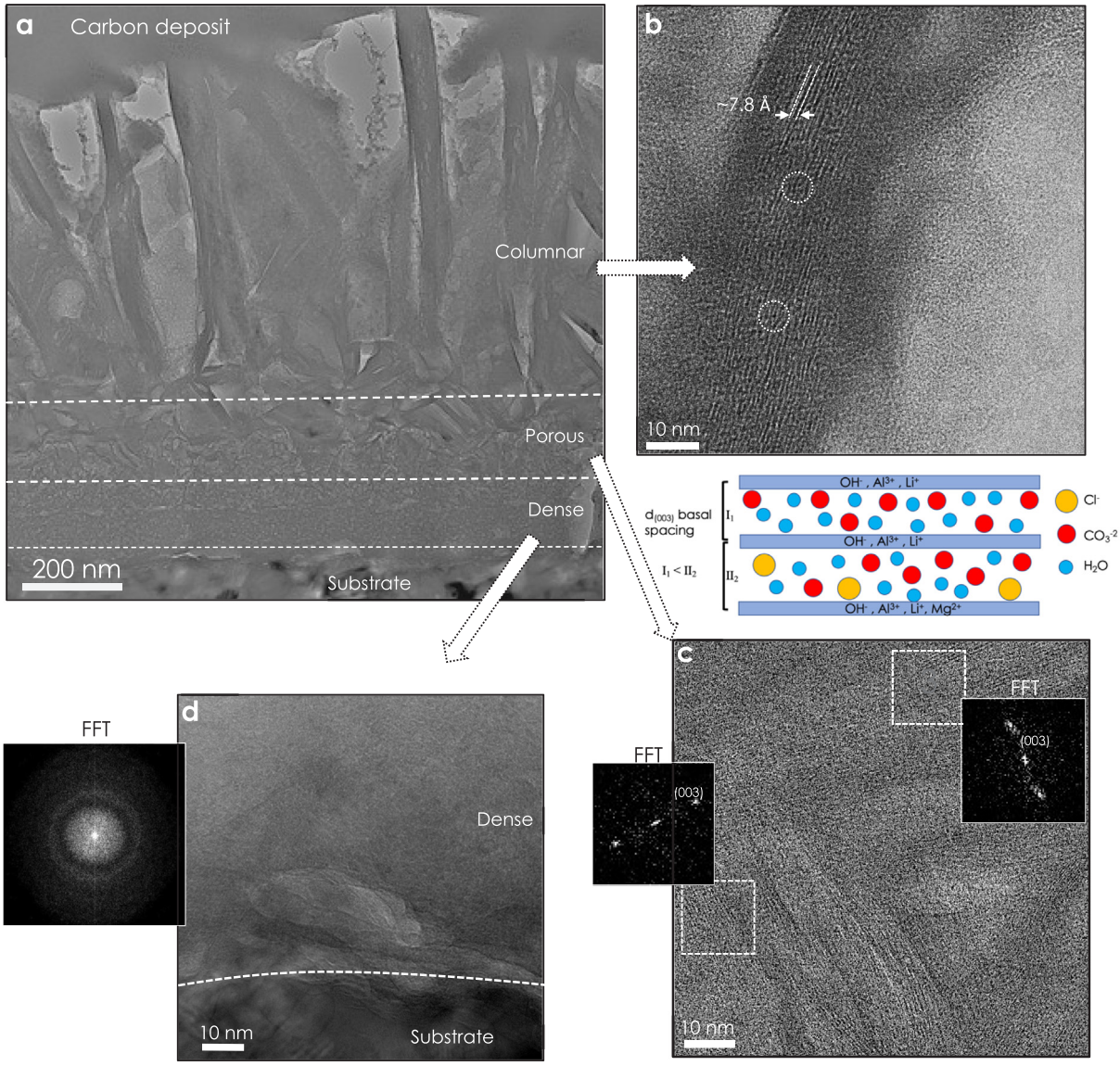


**Fig. 2.** (a) Cross-sectional TEM micrograph of the conversion layer formed in the peripheral region which is composed of three distinct sublayers. (b) HR-TEM image of an individual column, revealing the sandwich structure of the local phases. According to the d spacing, the structure represents Li-Al LDH; the circled regions are locations with crystal imperfections. The inset schematically shows a layered double hydroxide structure. (c) A closer look at the porous layer, revealing formation of Li-Al LDH but in a different morphology than columnar layer. The FFTs of the squared regions show interference spots corresponding to the (0 0 3) plane. (d) A zoomed-in image of the dense layer; the FFT pattern of the dense layer implies an amorphous structure.

elemental analysis of the porous layer/columnar layer interface discloses that lithium is present rather homogeneously over the different local phases, mostly matching to aluminum (see Fig. 3b). A map taken from a part of an individual column clearly reveals the presence of lithium in the form of layers while no Al and Li signals come from the interlayer spacing. As reported, there are no cations in the anionic part as aluminum and lithium are accommodated in the LDH sheets (i.e. (0 0 3) plane), see the inset in Fig. 2b.

### *3.2. Cross-sectional characterization of the layer formed in the middle region*

Fig. 4 shows structural TEM analysis of the conversion layer established in the middle region of the scribe. Compared to the peripheral region, the middle-region layer comprises an inner barrier layer with a heterogeneous morphology and a significantly thicker porous layer (ca. 400 nm) where the columnar part is missing (see Fig. 4a). It should be noted that the conversion layer formed in the middle area (approx. 500 nm) is thinner than that formed in the peripheral region of the scribe. HR-TEM imaging of the porous part of the conversion layer evidences the crystalline local phases within this sublayer, shown in Fig. 4b. Although a smaller d spacing has been measured (i.e. 7.2 Å), but it still implies the presence of Li-Al LDH. In addition, the appearance of the spots in the selected area electron diffraction (SAED) pattern shows that the porous layer is composed of co-existing crystalline and amorphous phases. Verified by the collected SAED pattern, the dense layer is structurally amorphous, as observed for the peripheral region, where roundish 5–20 nm porosities are also seen (see Fig. 4c). The porosity size increases with the distance from the substrate; the porosities in the porous layer are irregular in shape.

EF-TEM was used to see the distribution of lithium in the layer of the middle region. As shown in Fig. 5a, lithium is spread uniformly within the dense and porous layer similar to the peripheral region. Recently in a work, Visser et al. detected lithium throughout the 1-mm scribe, albeit at lower concentrations in the middle region [38]. However, the local lithium-poor products can hardly be distinguished in the

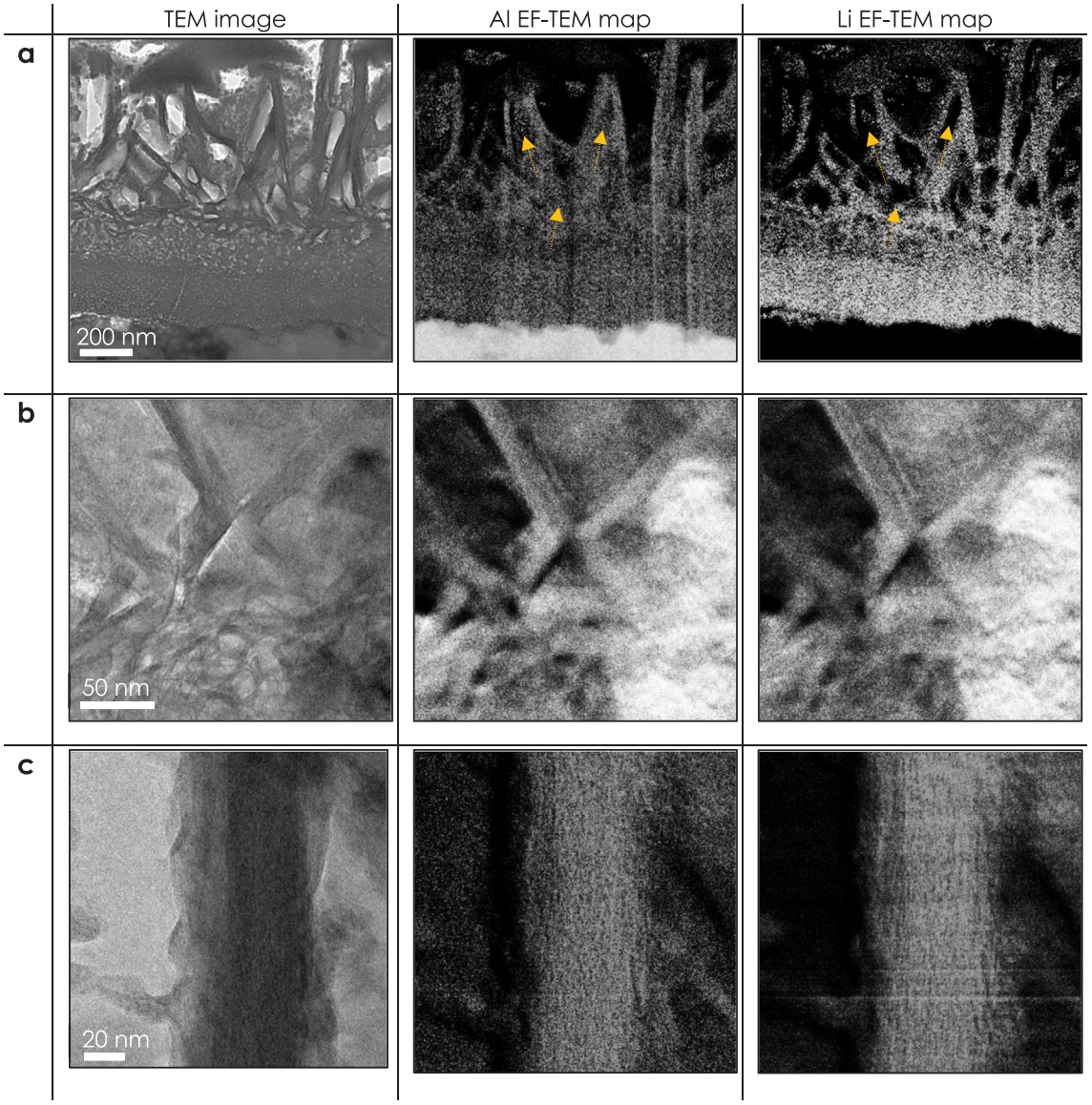


**Fig. 3.** Bright field TEM images and the corresponding EF-TEM maps of aluminum and lithium obtained at 300 keV; (a) the entire layer formed in the peripheral region; the yellow arrows indicate lithium-free region, (b) at columnar layer/porous layer interface and (c) an individual column in the top layer. Li K-edge and Al $L_{2,3}$-edge were filtered by putting 6-eV slits before and after the corresponding edges (jump-ratio technique), respectively.

EF-TEM lithium and aluminum maps which are the projection of the whole thickness. Moreover, EF-TEM maps are mainly intensity-based images with moderate detection limit and therefore inadequate to map elements present at low concentration. Thus, a high-sensitivity surface analysis is beneficial to determining the regions in the protective layer with high and low lithium concentration. For this reason, high resolution SIMS analysis was performed on a cross-section of the protective layer in the middle region. Because of possible artefacts that may arise near the peripheral areas (e.g. uneven electric field for secondary ion extraction), the SIMS analysis was limited to the middle region of the scribe. An overlay of $^{27}Al^+$ and $^{7}Li^+$ SIMS images is presented in Fig. 5b, revealing a higher lithium signal in the inner part of the conversion layer. The presence of lithium is detected rather intensely and uniformly in the inner part of the layer whereas partly observed in the top part. Fig. 5c shows the line profiles along the yellow arrow in Fig. 5b. As can be seen, Al and Li concentrations decrease toward the top part where the layer has a higher level of porosity. In addition, a maximum Li/Al ratio of ~0.05 is estimated within the dense amorphous layer close to the substrate (note the right-side y-axis of Fig. 5c). This shows that the amorphous inner layer products contain lithium, as qualitatively observed in the EF-TEM maps. On the other hand, the presence of the products with less lithium can be an indication of lithium concentration variation at different stages at which various local phases can exist.

### *3.3. Overall cross-sectional and lateral conversion layer formation mechanism*

The leaching of lithium carbonate occurs upon exposure of the coated and scribed panels to NSS, establishing a lateral concentration gradient of lithium and pH within the scribe (see Fig. 6) [14,17]. Presumably, the Li concentration and pH are also diverse in the direction perpendicular to the surface which can result in the formation of a multi-layered morphology and chemistry of the conversion layer at different locations of the scribe [38,39]. To establish a Li-Al conversion layer, lithium becomes available through the corrosion inhibitor leaching while aluminum is provided by the direct dissolution of the substrate. Scanning ion-selective electrode technique (SIET) measurements by Visser et al. [17] showed that the pH within the scribe rapidly goes up to 9.5 after 5 min of the exposure and stabilizes at approx. 9.7;

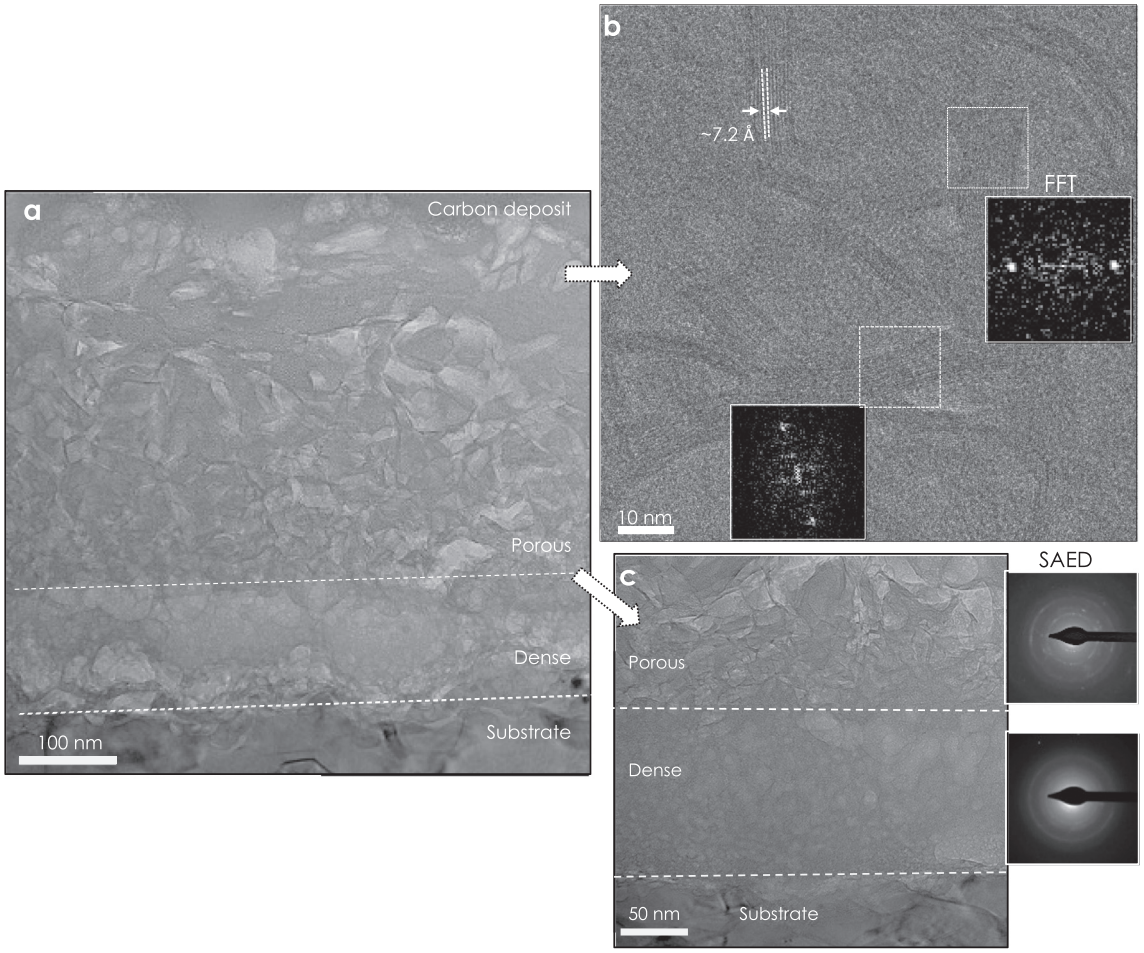


**Fig. 4.** (a) Cross-sectional TEM micrograph of the conversion layer formed in the middle region, comprising a dense and porous layer. (b) HR-TEM image and local FFTs of the porous layer, revealing local phases with Li-Al LDH characteristic. (c) A closer look at the dense and porous layer; nano-porosities are evident within the dense layer. SAED pattern reveals that the dense layer is amorphous whereas the porous layer is composed of amorphous and crystalline local phases.

such alkalinity is high enough to trigger active dissolution of the substrate as the aluminum oxide passive layer would be undermined and soluble $AlO_2^-$ would be stable. The lithium then starts to intercalate, resulting in the formation of stable corrosion products like Li-Al LDH. Through this simultaneous dissolution/precipitation process, the formation of the conversion layer may occur in the alkaline environment. For instance, the peripheral layer (Region I) appears in a columnar morphology as this region endures higher pH at which Li-Al LDH is merely stable [38]. Comparatively, in the middle part (Region II) a lower dissolution/precipitation ratio is expected as a result of a lower alkalinity, leading to the formation of a less porous layer that contains lithium free aluminum hydroxides.

As schematically shown in Fig. 6, closest to the substrate, a ubiquitous dense layer in which roundish nano-porosities are evident is formed. Visser et al. proved that this layer is the main contributor of the corrosion protection [18]. Considering all structural and chemical characterizations into account, the amorphous dense inner layer can be Li-pseudoboehmite in agreement with what Visser et al. identified previously using the reference samples [17]. Pseudoboehmite is known as an aluminum compound with the chemical composition AlO(OH); however, it is finely crystalline boehmite that contains a high amount of water [40]. The porous middle layer is quite diverse in chemical composition and morphology and characterized as a mixed layer of co-existing lithium free/containing amorphous and Li-Al LDH crystalline products. The porous outer layer formed in the middle part is twice thicker than that in the peripheral region. Considering the chemical composition of the layer, the lithium-free phase is mainly aluminum hydroxide whereas the amorphous Li-containing part can be Li-pseudoboehmite. The presence of lithium-free products can be an indication of local pH and Li concentration variation in which various corrosion products can remain stable. Establishment of a columnar morphology is directly ascribed to the solution chemistry experienced by the peripheral regions. According to the chemical composition of the layer, $[LiAl_2(OH)_6](CO_3)_{0.5}{\cdot}nH_2O$) is considered to be the most prominent product in the columnar layer, intercalation of $Cl^-$ in the anionic interlayer spacing can also lead to the formation of $[LiAl_2(OH)_6]Cl{\cdot}nH_2O$ or $[Li_{0.99}Al_{2.01}(OH)_6](CO_3)_{0.44}Cl_{0.01}{\cdot}nH_2O$ which have both a layered double hydroxide character.

## 4. Conclusions

In this study, the conversion layer generated on AA2024-T3 from a Li-leaching coating was fully characterized. This was achieved through successful analytical TEM and SIMS studies over the cross-sections of the entire layer formed at different locations of the scribe. It was shown that the conversion layer, regardless of the location in the scribe, is composed of an inner dense layer and a porous layer. The peripheral region which experiences higher pH and lithium concentrations during the exposure to a corrosive environment comprises an additional outer columnar layer. Lithium was found uniformly spread over the different sublayers, although the local phases with no/low concentration of lithium were also detected. The dense layer, approx. 100–150 nm thick, was specified as amorphous Li-incorporated aluminum hydroxides with a high amount of trapped water (named Li-pseudoboehmite). It was

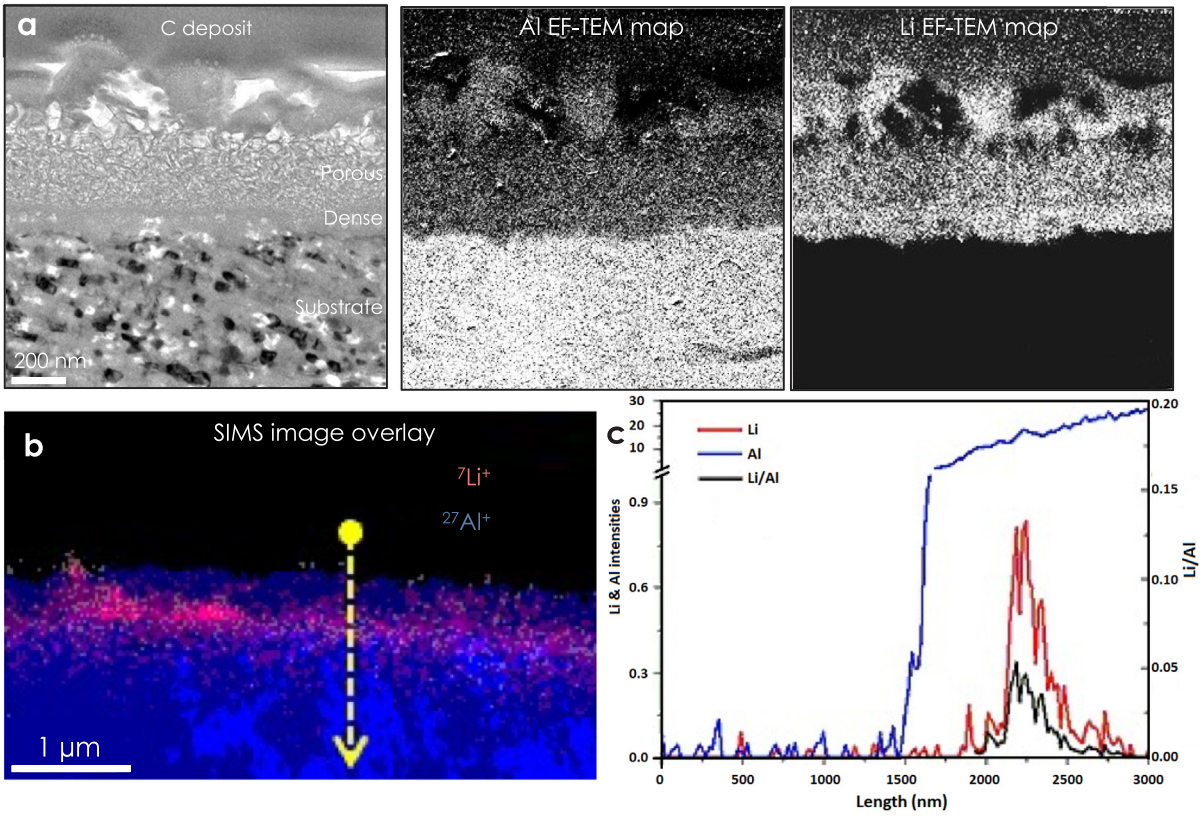


**Fig. 5.** (a) Bright field TEM images and the corresponding EF-TEM maps of aluminum and lithium obtained at 80 keV. (b) SIMS elemental distribution of Li and Al in the middle region. (c) Line elemental and Li/Al ratio profiles along the indicated arrow.

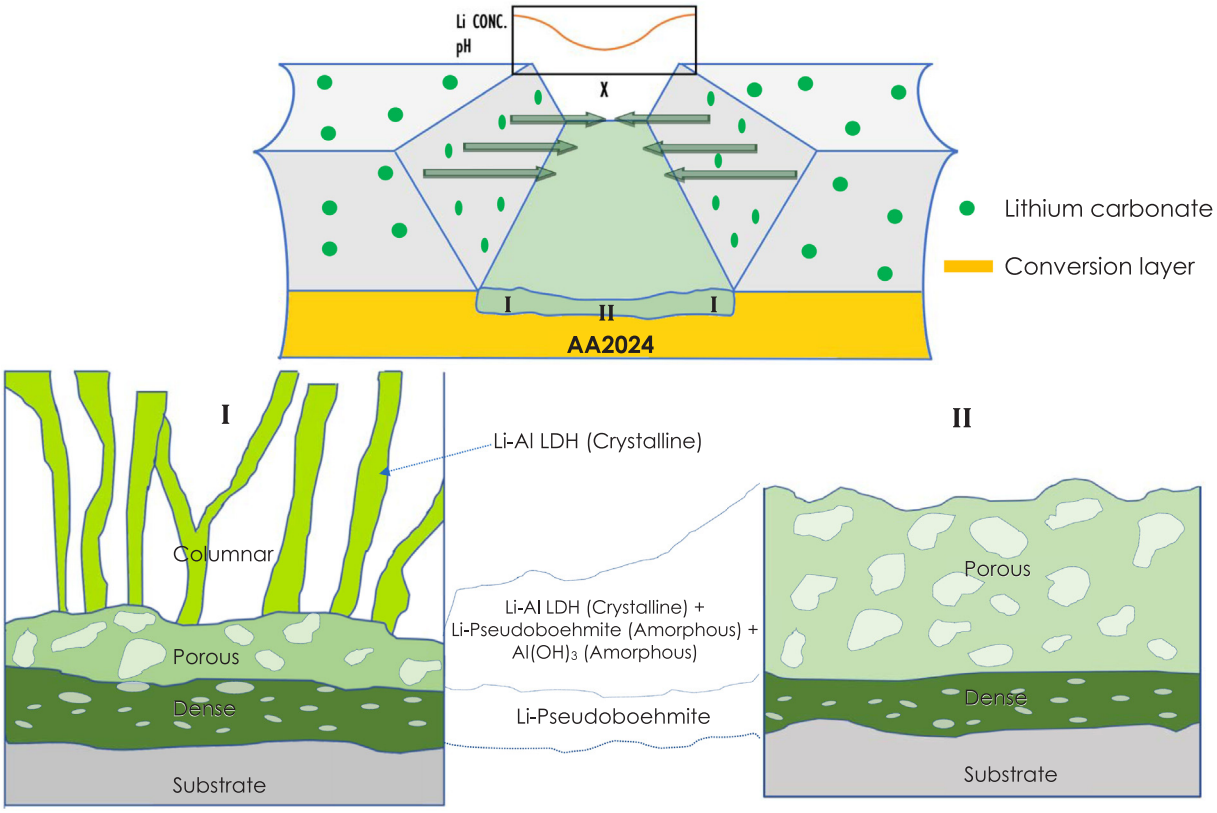


**Fig. 6.** Schematic representation of the lithium carbonate leaching from the coating, resulting in a lateral pH and Li concentration within the scribe. The scribe can be divided into peripheral (Region I) and middle (Region II) parts which experience different solution chemistry during the NSS exposure. The cross-sectional morphology of the formed layers is location-dependent and different local phases can be distinguished at the peripheral and middle region respectively.

shown that the columnar morphology is composed of single-crystal pillars of Li-Al LDH. This is a product of $CO_3^{2-}$, $H_2O$ and even $Cl^-$ intercalation between the $d_{(003)}$ planes which contains $Al^{3+}$, $Li^+$ and $OH^-$, leading to a sandwich structure. Crystal imperfections were also observed within the structure. The porous layer, shown to be thicker in the middle region, consists of co-existing amorphous and crystalline compounds. The crystalline products are Li-Al LDH while the amorphous products may comprise different concentration of lithium. Crystallization of the amorphous dense layer and removal of interlayer water from the Li-Al LDH structure were observed under the electron beam but could competently be avoided through a low-dose imaging.

## CRediT authorship contribution statement

**A. Kosari:** Investigation, Writing - original draft. **P. Visser:** Investigation, Writing - review & editing. **F. Tichelaar:** Investigation, Writing - review & editing. **S. Eswara:** Investigation. **J-N. Audinot:** Investigation. **T. Wirtz:** Investigation. **H. Zandbergen:** Supervision, Writing - review & editing. **H. Terryn:** Supervision, Writing - review & editing. **J.M.C. Mol:** Supervision, Writing - review & editing.

## Declaration of Competing Interest

The authors declare that they have no known competing financial interests or personal relationships that could have appeared to influence the work reported in this paper.

## Acknowledgement

The authors thank AkzoNobel for financially supporting this work under project number UPON B2 14205, Nederlandse Organisatie voor Wetenschappelijk Onderzoek (NWO). This work was co-funded by the Luxembourg National Research Fund (FNR) through grant INTER/SNF/16/11536628 (NACHOS).

## Appendix A. Supplementary material

Supplementary data to this article can be found online at https://doi.org/10.1016/j.apsusc.2020.145665.

## References

[1] A. Boag, R. Taylor, T. Muster, N. Goodman, D. McCulloch, C. Ryan, B. Rout, D. Jamieson, A. Hughes, Stable pit formation on AA2024-T3 in a NaCl environment, Corros. Sci. 52 (2010) 90–103.
[2] A.E. Hughes, R. Parvizi, M. Forsyth, Microstructure and corrosion of AA2024, Corros. Rev. 33 (2015) 1–30.
[3] N. Birbilis, Y. Zhu, S. Kairy, M. Glenn, J.-F. Nie, A. Morton, Y. Gonzalez-Garcia, H. Terryn, J. Mol, A. Hughes, A closer look at constituent induced localised corrosion in Al-Cu-Mg alloys, Corros. Sci. 113 (2016) 160–171.
[4] M. Kendig, R. Buchheit, Corrosion inhibition of aluminum and aluminum alloys by soluble chromates, chromate coatings, and chromate-free coatings, Corrosion 59 (2003) 379–400.
[5] M. Kendig, S. Jeanjaquet, R. Addison, J. Waldrop, Role of hexavalent chromium in the inhibition of corrosion of aluminum alloys, Surf. Coat. Technol. 140 (2001) 58–66.
[6] L. Xia, E. Akiyama, G. Frankel, R. McCreery, Storage and release of soluble hexavalent chromium from chromate conversion coatings equilibrium aspects of Cr VI concentration, J. Electrochem. Soc. 147 (2000) 2556–2562.
[7] A.E. Hughes, I.S. Cole, T.H. Muster, R.J. Varley, Designing green, self-healing coatings for metal protection, NPG Asia Mater. 2 (2010) 143–151.
[8] O. Gharbi, S. Thomas, C. Smith, N. Birbilis, Chromate replacement: what does the future hold? npj Mater. Degrad. 2 (2018) 1–8.
[9] J. Fernandes, M. Ferreira, Effect of carbonate and lithium ions on the corrosion performance of pure aluminium, Electrochim. Acta 37 (1992) 2659–2661.
[10] C. Rangel, M. Travassos, The passivation of aluminium in lithium carbonate/bicarbonate solutions, Corros. Sci. 33 (1992) 327–343.
[11] R.G. Buchheit, M. Bode, G. Stoner, Corrosion-resistant, chromate-free talc coatings for aluminum, Corrosion 50 (1994) 205–214.
[12] C. Drewien, M. Eatough, D. Tallant, C. Hills, R. Buchheit, Lithium-aluminum-carbonate-hydroxide hydrate coatings on aluminum alloys: Composition, structure, and processing bath chemistry, J. Mater. Res. 11 (1996) 1507–1513.
[13] P. Visser, S.A. Hayes, WO2010112605-A1, 2010.
[14] Y. Liu, P. Visser, X. Zhou, S.B. Lyon, T. Hashimoto, M. Curioni, A. Gholinia, G.E. Thompson, G. Smyth, S.R. Gibbon, Protective film formation on AA2024-T3 Aluminum Alloy by leaching of lithium carbonate from an organic coating, J. Electrochem. Soc. 163 (2016) C45–C53.
[15] P. Visser, Y. Liu, H. Terryn, J. Mol, Lithium salts as leachable corrosion inhibitors and potential replacement for hexavalent chromium in organic coatings for the protection of aluminum alloys, J. Coat. Technol. Res. 13 (2016) 557–566.
[16] P. Visser, Y. Liu, X. Zhou, T. Hashimoto, G.E. Thompson, S.B. Lyon, L.G. van der Ven, A.J. Mol, H.A. Terryn, The corrosion protection of AA2024-T3 aluminium alloy by leaching of lithium-containing salts from organic coatings, Faraday Discuss. 180 (2015) 511–526.
[17] P. Visser, A. Lutz, J. Mol, H. Terryn, Study of the formation of a protective layer in a defect from lithium-leaching organic coatings, Prog. Org. Coat. 99 (2016) 80–90.
[18] P. Visser, M. Meeusen, Y. Gonzalez-Garcia, H. Terryn, J.M. Mol, Electrochemical evaluation of corrosion inhibiting layers formed in a defect from lithium-leaching organic coatings, J. Electrochem. Soc. 164 (2017) C396–C406.
[19] K. Marcoen, P. Visser, G. Trindade, M.-L. Abel, J. Watts, J. Mol, H. Terryn, T. Hauffman, Compositional study of a corrosion protective layer formed by leachable lithium salts in a coating defect on AA2024-T3 aluminium alloys, Prog. Org. Coat. 119 (2018) 65–75.
[20] S. Basak, J. Jansen, Y. Kabiri, H.W. Zandbergen, Towards optimization of experimental parameters for studying Li-O2 battery discharge products in TEM using in situ EELS, Ultramicroscopy 188 (2018) 52–58.
[21] S. Muto, K. Tatsumi, Detection of local chemical states of lithium and their spatial mapping by scanning transmission electron microscopy, electron energy-loss spectroscopy and hyperspectral image analysis, Microscopy 66 (2016) 39–49.
[22] J.S. Laird, A.E. Hughes, C.G. Ryan, P. Visser, H. Terryn, J. Mol, Particle induced gamma and X-ray emission spectroscopies of lithium based alloy coatings, Nucl. Instrum. Meth. Phys. Res., Sect. B 404 (2017) 167–172.
[23] P. Visser, H. Terryn, J.M.C. Mol, Aerospace coatings, in: A.E. Hughes, J.M.C. Mol, M.L. Zheludkevich, R.G. Buchheit (Eds.), Active Protective Coatings: New-Generation Coatings for Metals, Springer, Netherlands, Dordrecht, 2016, pp. 315–372.
[24] D. Dowsett, T. Wirtz, Co-registered in situ secondary electron and mass spectral imaging on the helium ion microscope demonstrated using lithium titanate and magnesium oxide nanoparticles, Anal. Chem. 89 (2017) 8957–8965.
[25] P. Gratia, I. Zimmermann, P. Schouwink, J.-H. Yum, J.-N. Audinot, K. Sivula, T. Wirtz, M.K. Nazeeruddin, The many faces of mixed ion perovskites: unraveling and understanding the crystallization process, ACS Energy Lett. 2 (2017) 2686–2693.
[26] T. Wirtz, O. De Castro, J.-N. Audinot, P. Philipp, Imaging and analytics on the helium ion microscope, Annu. Rev. Anal. Chem. 12 (2019) 523–543.
[27] L. Li, R. Ma, Y. Ebina, K. Fukuda, K. Takada, T. Sasaki, Layer-by-layer assembly and spontaneous flocculation of oppositely charged oxide and hydroxide nanosheets into inorganic sandwich layered materials, J. Am. Chem. Soc. 129 (2007) 8000–8007.
[28] S. Nagendran, G. Periyasamy, P.V. Kamath, Structure models for the hydrated and dehydrated nitrate-intercalated layered double hydroxide of Li and Al, Dalton Trans. 45 (2016) 18324–18332.
[29] J. Thiel, C. Chiang, K.R. Poeppelmeier, Structure of lithium aluminum hydroxide dihydrate ($LiAl_2$ (OH) 7.2 $H_2O$), Chem. Mater. 5 (1993) 297–304.
[30] J.L. Gunjakar, T.W. Kim, H.N. Kim, I.Y. Kim, S.-J. Hwang, Mesoporous layer-by-layer ordered nanohybrids of layered double hydroxide and layered metal oxide: highly active visible light photocatalysts with improved chemical stability, J. Am. Chem. Soc. 133 (2011) 14998–15007.
[31] I.C. Chisem, W. Jones, Ion-exchange properties of lithium aluminium layered double hydroxides, J. Mater. Chem. 4 (1994) 1737–1744.
[32] M. Yasaei, M. Khakbiz, E. Ghasemi, A. Zamanian, Synthesis and characterization of ZnAl-$NO_3$ (-$CO_3$) layered double hydroxide: A novel structure for intercalation and release of simvastatin, Appl. Surf. Sci. 467 (2019) 782–791.
[33] S.P. Newman, W. Jones, Synthesis, characterization and applications of layered double hydroxides containing organic guests, New J. Chem. 22 (1998) 105–115.
[34] M.-C. Lin, F.-T. Chang, J.-Y. Uan, Synthesis of Li–Al-carbonate layered double hydroxide in a metal salt-free system, J. Mater. Chem. 20 (2010) 6524–6530.
[35] V. Rives, Layered Double Hydroxides: Present and Future, Nova Publishers, 2001.
[36] X. Hou, D.L. Bish, S.-L. Wang, C.T. Johnston, R.J. Kirkpatrick, Hydration, expansion, structure, and dynamics of layered double hydroxides, Am. Mineral. 88 (2003) 167–179.
[37] G. Choi, H. Piao, Z.A. Alothman, A. Vinu, C.-O. Yun, J.-H. Choy, Anionic clay as the drug delivery vehicle: tumor targeting function of layered double hydroxide-methotrexate nanohybrid in C33A orthotopic cervical cancer model, Int. J. Nanomed. 11 (2016) 337–348.
[38] P. Visser, K. Marcoen, G. Trindade, M. Abel, J. Watts, T. Hauffman, J. Mol, H. Terryn, The chemical throwing power of lithium-based inhibitors from organic coatings on AA2024-T3, Corros. Sci. 150 (2019) 194–206.
[39] P. Visser, Y. Gonzalez-Garcia, J.M. Mol, H. Terryn, Mechanism of passive layer formation on AA2024-T3 from alkaline lithium carbonate solutions in the presence of sodium chloride, J. Electrochem. Soc. 165 (2018) C60–C70.
[40] B. Baker, R. Pearson, Water content of pseudoboehmite: A new model for its structure, J. Catal. 33 (1974) 265–278.